Nanoscale Horizons

ROYAL SOCIETY OF CHEMISTRY

COMMUNICATION

View Article Online
View Journal

Cite this: DOI: 10.1039/d5nh00285k

Received 29th April 2025,
Accepted 5th September 2025

DOI: 10.1039/d5nh00285k

rsc.li/nanoscale-horizons

Flexible MXene–cellulose nanofiber based all-solid-state supercapacitors with high volumetric capacitance

Yongzan Zhou,[a] Youchao Teng, *[a] Huicong Liu *[b] and Yimin Wu *[a]

All-solid-state supercapacitors (ASSCs) are critical for next-generation flexible and wearable electronic devices, but their development has been hindered by the challenge of balancing high energy storage performance with mechanical flexibility in wearable energy storage systems. MXene materials offer excellent electrical conductivity, large surface area, and outstanding charge storage capability, but their application in flexible devices is limited by poor mechanical stability and structural degradation. To overcome these challenges, we have developed MXene/cellulose nanofiber (CNF) composites. CNF is a cheap and environmentally friendly material with a huge storage capacity on earth. The doping of CNFs into a layered MXene material prevents the stacking of the MXene, improves the ionic transport speed, maintains the excellent electrochemical properties of the MXene, and enhances the structural reinforcement and flexibility. The flexible, binder-free ASSCs have excellent electrochemical properties with a volumetric capacitance of 94.21 F cm^{-3}. The electrochemical properties also showed no degradation in bending tests in the range of 30°–120°. The capacitance retention was 97.87% after 10 000 bending cycles at an angle of 60°. This work provides a scalable and green approach to fabricating high-performance MSCs and points the way to the next generation of wearable electronics.

[a] *Department of Mechanical and Mechatronics Engineering, and Waterloo Institute for Nanotechnology, Materials Interfaces Foundry, University of Waterloo, Waterloo, Canada. E-mail: youchao.teng@uwaterloo.ca, yimin.wu@uwaterloo.ca*

[b] *School of Mechanical and Electrical Engineering, Soochow University, Suzhou 215123, China. E-mail: hcliu078@suda.edu.cn*

Yimin Wu

Congratulations on the 10th year anniversary of Nanoscale Horizons! Nanoscale Horizons has always been at the frontier of nanotechnology and materials science. We have been publishing in Nanoscale Horizons since 2019. We are proud to continue to contribute to this excellent journal. We are thrilled to contribute this article that shows a new strategy to design flexible all-solid-state supercapacitors (ASSCs) by compositing 2D MXene nanosheets with sustainable cellulose nanofibers (CNFs) as flexible, wearable, and energy storage devices for Internet-of-Things applications. Looking forward to seeing what nanotechnology and materials science can shape the world.

New concepts

This study presents a new strategy to design flexible all-solid-state supercapacitors (ASSCs) by compositing 2D MXene nanosheets with cellulose nanofibers (CNFs). Despite their excellent conductivity and capacitance performance, MXenes often suffer from poor mechanical flexibility and structural collapse in flexible devices. The novelty of this work lies in the introduction of a sustainable and low-cost material with good environmental compatibility, cellulose nanofiber (CNF) material, as the intercalation structure, which effectively prevents MXene interlayer stacking, improves the ion transport efficiency, and enhances the mechanical stability of the device. Unlike previous strategies that rely on complex structures or polymer binders, our approach combines spin-coating and photolithography to achieve a simple, scalable and efficient fabrication process. Benefiting from this design, the ASSC displays a high volumetric capacitance of 94.21 F cm^{-3} and excellent electrochemical stability, retaining 97.87% of its initial capacitance after 10 000 cycles at a bending angle of 60°. In addition, the device has a volumetric energy density of 3.27 mWh cm^{-3} and a power density of 0.25 W cm^{-3}, demonstrating its strong energy storage capability under mechanical deformation conditions. This work provides valuable insights into the structural engineering of 2D materials and suggests a promising strategy for advancing flexible, wearable, and energy storage devices designed for IoT applications.

Introduction

The advancement of flexible and wearable electronics demands energy storage devices that not only deliver high performance

but also maintain mechanical flexibility. Supercapacitors, with their high power density, long cycle life, and rapid charge–discharge capabilities, have emerged as essential components for next-generation portable electronics.[1–4] With the rapid growth of the Internet of Things (IoT), flexible all-solid-state supercapacitors (ASSCs) are attracting a lot of attention. They are small, lightweight, reliable and easy to handle. The flexible design makes them adaptable to a wide range of smart devices, providing an ideal energy storage solution for IoT devices.[5–7] Despite recent advances, ASSCs still face significant challenges in achieving high specific capacitance. Limited electronic conductivity and restricted ionic transport limit their rate capability and capacitance storage. Meanwhile, mechanical flexibility and poor cycling stability under operating stress further prevent their practical application.[8,9]

MXene materials are a class of two-dimensional transition metal carbides and nitrides, and most of the current fabrication methods for Mxenes are the etching of aluminum atoms.[10] Due to their excellent electrical conductivity, wide surface area, and excellent electrochemical properties, MXenes have become highly promising candidate materials. Despite these advantages, MXenes are inherently mechanically brittle due to weak interlayer bonding and a lack of solid structural support.[11] This brittleness is exacerbated under mechanical stress, which induces delamination and microcrack formation, ultimately affecting device performance. To fully realize the potential of MXenes in flexible electronics, these shortcomings must be addressed. To mitigate these challenges, several approaches have been explored.

MXene nanosheets are typically prepared as flexible thin films by vacuum filtration, coating and 3D printing techniques. However, these films are prone to self-stacking, limit ion transport and are less flexible.[12–15] To address these issues, MXene nanosheets have been fabricated into fibers using wet spinning or electrospinning techniques to enhance the flexibility, ionic accessibility, and electrochemical properties of the materials. Although the overall performance is excellent, the manufacturing cost is high and the precision is low, which cannot meet the requirements as a new type of micro energy storage device.[16–21] Alternatively, compositing MXenes with flexible conductive polymers (*e.g.*, polyaniline (PANI)[22] and polypyrrole (PPy)[23]) and carbon-based materials (*e.g.*, graphene[24] and carbon nanotubes (CNTs)[25]), combined with structural design strategies such as intercalation or porous architectures, can effectively mitigate the self-stacking problem, enhance the conductive network, and improve flexibility. This is the current optimal solution, which effectively balances the performance requirements of high flexibility and high capacitance.[26,27]

Conductive polymers and carbon-based materials excel as functional materials. However, challenges such as their complex synthesis processes, high production costs, and environmental concerns have limited their large-scale industrial applications. In contrast, cellulose nanofibers (CNFs) derived from renewable resources offer a sustainable and cost-effective alternative. Their unique fiber structure enhances ionic transport and electrochemical activity within the MXene layer. Moreover, CNFs exhibit excellent mechanical flexibility and strong interfacial compatibility, which significantly improve the structural stability of MXene composites under mechanical deformation.[28] These advantages make CNFs ideal for the development of high-performance, environmentally friendly MXene-based electrodes, which have great potential, especially in flexible energy storage devices. Table S1 shows a summary of the modification strategies and key parameters of MXene supercapacitors in recent years and a comparison with this study. In this study, we fabricated MXene/CNF composite thin films and evaluated their viability for flexible ASSC applications. By systematically optimizing the MXene-to-CNF ratio, we identified an optimal composition, 50% CNF, which demonstrated a volumetric capacitance of 94.21 F cm^{-3} and preserved 97.87% of its capacitance after 10 000 bending cycles at an angle of 60°. The fabrication process, incorporating photolithography-based ion milling techniques, enabled the precise development of interdigitated electrode configurations, ensuring scalability and uniformity. These devices exhibited remarkable volumetric capacitance, robust cycling stability, and reliable performance across various mechanical deformation scenarios. This work underscores the transformative potential of MXene/CNF composites in the domain of flexible and wearable energy storage. Compared to traditional materials such as graphene and carbon-based composites, MXene/CNF composites offer a distinctive combination of enhanced volumetric capacitance and mechanical flexibility. By harmonizing structural reinforcement with innovative electrode engineering, this study establishes a foundational framework for the development of high-performance ASSCs, advancing their applicability in wearable electronics and the Internet of Things (IoT).

Experimental section

Preparation of materials

Chemical reagents, including hydrochloric acid (HCl), lithium fluoride (LiF), the Ti_3AlC_2 precursor, nanocellulose crystals (CNCs), nanocellulose fibers, sulfuric acid (H_2SO_4), potassium hydroxide (KOH), polyvinyl alcohol (PVA), polyethylene terephthalate (PET) film, and 1-ethyl-3-methylimidazolium acetate (EMImAc) ionic liquid, were procured from Sigma-Aldrich Chemical Company and used without further purification. All experimental chemicals were of reagent grade.

To prepare MXene dispersions, 1.6 g of LiF was mixed with 20 mL of 9 M HCl solution and stirred vigorously in a beaker for 30 minutes. Gradually, 1 g of Ti_3AlC_2 precursor was added to the mixture over 10 minutes to avoid strong exothermic reactions. The solution was then stirred in a 35 °C water bath for 72 hours. The resulting mixture was centrifuged with distilled water at 5000 rpm, and the supernatant was separated from the precipitate. The precipitate was washed with deionized water and centrifuged repeatedly until the supernatant reached a neutral pH. After sonication for 15 minutes, the mixture was centrifuged at 3000 rpm for 1 hour to obtain the desired upper

dispersion.[29] The supernatant was the MXene solution. Pure MXene membranes were produced by filtration and used as a blank control group for comparing electrochemical properties with CNF-added groups.

Fabrication of an MXene/CNF composite thin film

The initial example employed a composite film of MXene/CNF in a ratio of 1 : 0.5. Controlling the total mass of solutes at 100 mg, 66 mg of MXene and 33 mg of CNF were taken into 20 mL of water and stirred at room temperature for 12 h, followed by ultrasonic dispersion for 30 min to obtain a homogeneous solution. The fabrication process of the MXene/CNF composite thin-film supercapacitor is illustrated in Fig. 1a–d. The mixed solution was filtered through a nitrocellulose membrane filter (pore size 0.22 μm) in a vacuum filtration unit at −0.9 bar for 24 h to form a gel, which was then dried in a vacuum oven at 70 °C for 12 h. Four types of films were fabricated using a consistent procedure: a pristine MXene film (PM), and three MXene/CNF composites with mass ratios of 1 : 0.25, 1 : 0.5, and 1 : 0.75, denoted as M/C-0.25, M/C-0.5, and M/C-0.75, respectively. The composite electrodes were cut into 1 × 1 cm pieces and employed directly in aqueous supercapacitors. The electrochemical properties of the material were investigated using 6 M KOH as the electrolyte.

Fabrication of flexible MXene/CNF ASSCs

Fig. 1(e–h) shows the fabrication process of SSCs. The composited solution preparation process follows a method consistent with aqueous supercapacitors. To achieve flexibility and stability, PET plastic films were selected as the electrode substrate due to their excellent mechanical properties. The PET films were first cut to the desired size and ultrasonically cleaned in acetone and deionized water for 5 minutes each. To improve surface adhesion, PET films underwent oxygen ion surface treatment using reactive ion etching (RIE) under the following conditions: The radiofrequency power is 500 watts, the pressure is 800 millimeters of mercury (mTorr), the temperature is 25 degrees Celsius, the oxygen flow rate is 50 standard cubic centimeters per minute (sccm), and the treatment time is 600 seconds. Subsequently, a mixed MXene/CNF solution was spin-coated onto the treated PET substrate at a low rotation speed of 1000 rpm for 30 seconds, repeated three times to ensure uniform coverage. The films were then dried on a hot plate at 90 °C for 10 minutes to form a stable thin film. To enhance conductivity and protect the underlying electrode material, a 10 nm gold layer was deposited using magnetron sputtering. Then, a custom-designed shadow mask was placed over the film. The DIY mask is a 2 mm thick PET plastic plate coated with 3 μm Cr to avoid cross-contamination. Pattern formation is achieved through physical dry etching, specifically using ion milling technology. In this process, argon gas accelerates and hits the surface at a perpendicular angle (90°). The etching conditions include: a gas flow rate of 20 sccm, an ion source voltage of 400 V, a current of 410 mA, and a chamber pressure of 20 mTorr. Exposed regions were precisely resulting in well-defined interdigitated electrodes. Solid-state supercapacitors were prepared using two solid-state electrolytes: 1 M H_2SO_4/PVA and 80 wt% ionic liquid (IL)/PVA. This gel electrolyte is prepared by dissolving 1 M H_2SO_4 in a 10 wt% aqueous PVA solution and heating and stirring until a homogeneous gel is formed. After cooling, we covered the inserted electrode area with it by the spin-coating technique (1000 rpm for 30 s). The

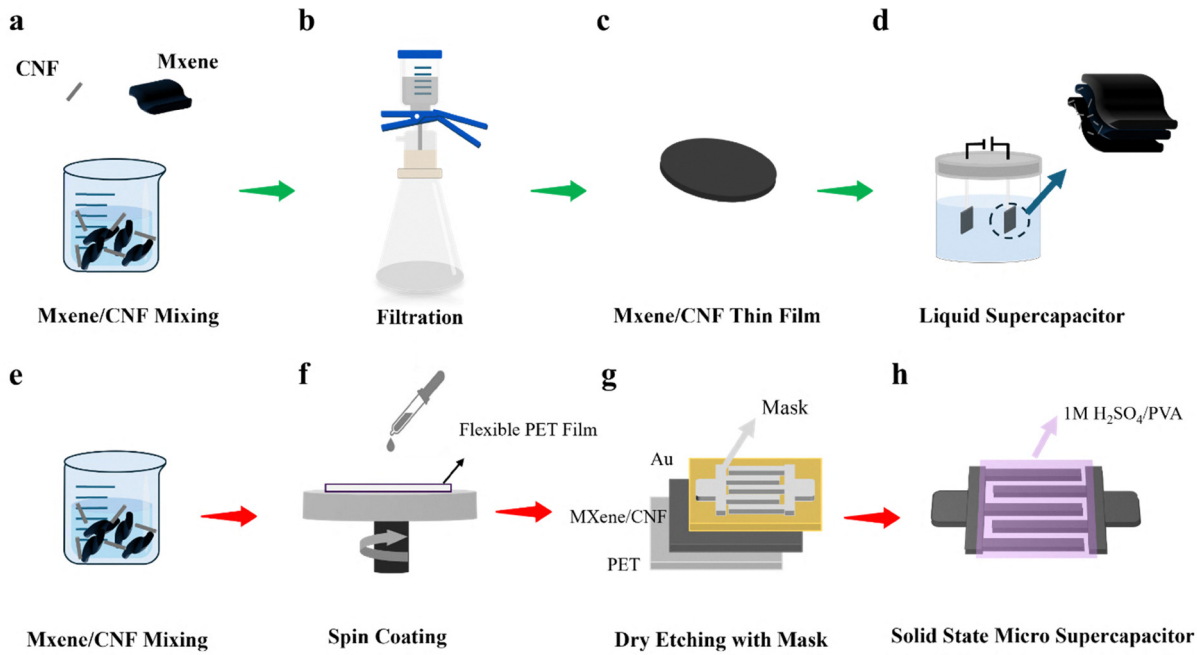

Fig. 1 Schematic of the fabrication process for MXene/CNF composite thin film supercapacitors, (a)–(d) represent the aqueous device, (e)–(h) represent the all-solid-state micro-supercapacitor using a H_2SO_4/PVA or ionic liquid (IL)/PVA gel electrolyte.

preparation method for IL/PVA gel electrolytes is the same as above, but 80% (mass fraction) EMIMAc is used instead of H_2SO_4.

Characterization of MXene/CNF composite thin films

The surface morphology and the presence of compounds in the samples were examined using a field emission SEM system (JEOL JSM-7200F) with an acceleration voltage of 10 kV. Material elemental maps were tested through an energy dispersive X-ray spectroscopy (EDS) system (Oxford). The crystal structure and the crystalline size of the samples were collected using an ARL X'TRA Powder XRD System (Thermo Scientific) using Cu Kα radiation, $l \approx 1.5406$ Å, 40 kV, 40 mA, at a scan speed of 5° min^{-1} with a step size of 0.02. The BET surface area of the material was calculated using a Micromeritics Gemini VII 2390a surface area analyzer with nitrogen as the adsorbent at 77 K over a range of relative pressures p/p° = 0.05–0.30.

To investigate the structural changes of Mxene/CNF composite thin films after doping with nanofibers, we calculated the interlayer spacing (*c*-axis lattice parameter, *c*-lattice parameter) based on the position of the (002) diffraction peaks in the X-ray diffraction (XRD) patterns. The analysis is based on Bragg's Law, and since for the layered material MXene, the (002) crystal plane reflects half of the layer spacing, the complete *c*-axis lattice constant can be expressed as eqn (1):

$$c = 2d = \frac{n\lambda}{\sin\theta} \tag{1}$$

All electrochemical characterization studies were measured using Gamry Interface 1010 (Gamry Instruments, USA).

Specific capacitance (C_s) was calculated from the cyclic voltammetry (CV) curves, according to eqn (2):

$$C_s = \frac{\int I(V)\mathrm{d}V}{v \times \Delta V \times X} \tag{2}$$

where $I(V)$ is the areal or volumetric current (mA), $\int I(V)\mathrm{d}V$ is the integrated area of the CV curve, v stands for the scan rate (mV s^{-1}), and ΔV (V) represents the voltage window. X represents the specific property used for normalization, which could be the electrode's surface area (C_a, mF cm^{-2}), volume (C_v, mF cm^{-3}) and mass (C_m, mF g^{-1}).

Specific capacitance (C_s) could also be calculated from the Galvanostatic charge–discharge (GCD) curves using eqn (3):

$$C_s = \frac{I \times \Delta t}{\Delta V \times X} \tag{3}$$

where I represent discharge current (mA cm^{-2}), and Δt refers to the duration (s) of the discharge process.

The corresponding energy density (E, Wh cm^{-3}) was calculated according to eqn (4):

$$E = \frac{C \times \Delta V^2}{7200} \tag{4}$$

Power density (P, W cm^{-3}) was calculated according to eqn (5):

$$P = \frac{E \times 3600}{\Delta t} \tag{5}$$

Cyclic voltammetry (CV) tests were executed with varying scan rates from 5 to 100 mV s^{-1}. Electrochemical impedance spectroscopy (EIS) measurements involved applying an amplitude of 1 mV and operating over a frequency span of 0.01 Hz to 100 kHz. To evaluate long-term stability, galvanostatic charge–discharge (GCD) tests were performed at a high current density of 3 mA cm^{-2}.

Results and discussion

Material characterization

In our initial experiments, we used two different celluloses, nanocellulose crystals (CNCs) and nanocellulose fibers. To evaluate the flexibility of the composite films, we controlled the CNF or CNC mass ratio at 50% and fabricated both films by vacuum filtration. Optical images of the MXene/CNC and MXene/CNF films are shown in Fig. S1. The MXene/CNC films were very inflexible, cracking and breaking upon drying. In contrast, the MXene/CNF film showed excellent flexibility and mechanical integrity, retaining its structure even after repeated bending or folding. This is because the rigidity and short dimensions of CNCs make it difficult to form an effective flexible network, whereas the long fiber structure and good network forming ability of CNFs enable them to disperse stresses and enhance the flexibility of the film. Fig. 2 is the cross-sectional and top-view SEM images of MXene/CNF composite films prepared by vacuum filtration with different CNF mass ratios (0.25, 0.5, and 0.75, corresponding to rows 1, 2, and 3, respectively). In the cross-sectional images (Fig. 2a, b, e, f, i and j), all the samples show a clear laminar structure, with the CNFs distributed and intercalated in the laminar Mxene. The formation of this laminar interwoven network structure reduces the stacking of MXenes. With the increase of the CNF mass ratio, the aggregation of CNFs in and on the MXene lamellae increased significantly. In the M/C-0.5 samples (Fig. 2e and f), CNFs are almost uniformly intercalated in the MXene lamellae, and the amount of CNFs agglomerated on the surface is less than that in M/C-0.75. The intercalation of an appropriate amount of CNFs can effectively improve the accessibility of the active surface of the electrode material and promote the charge transfer. The cross-sectional images show the uniform laminar structure of the film, with CNFs uniformly intercalated in the MXene layered structure. This uniform distribution helps to increase the active surface area of the electrode film and enhance its electrical conductivity and adsorption properties. Top-view SEM images (Fig. 2c, g and k) and high magnification images (Fig. 2d, h and l) further explain the changes in surface morphology with an increase in CNF mass ratio. At a low CNF ratio (M/C-0.25), the CNF network is relatively dilute and part of the surface of the MXene sheet is exposed. When the CNF mass ratio is increased to 0.5, most of the CNFs are uniformly

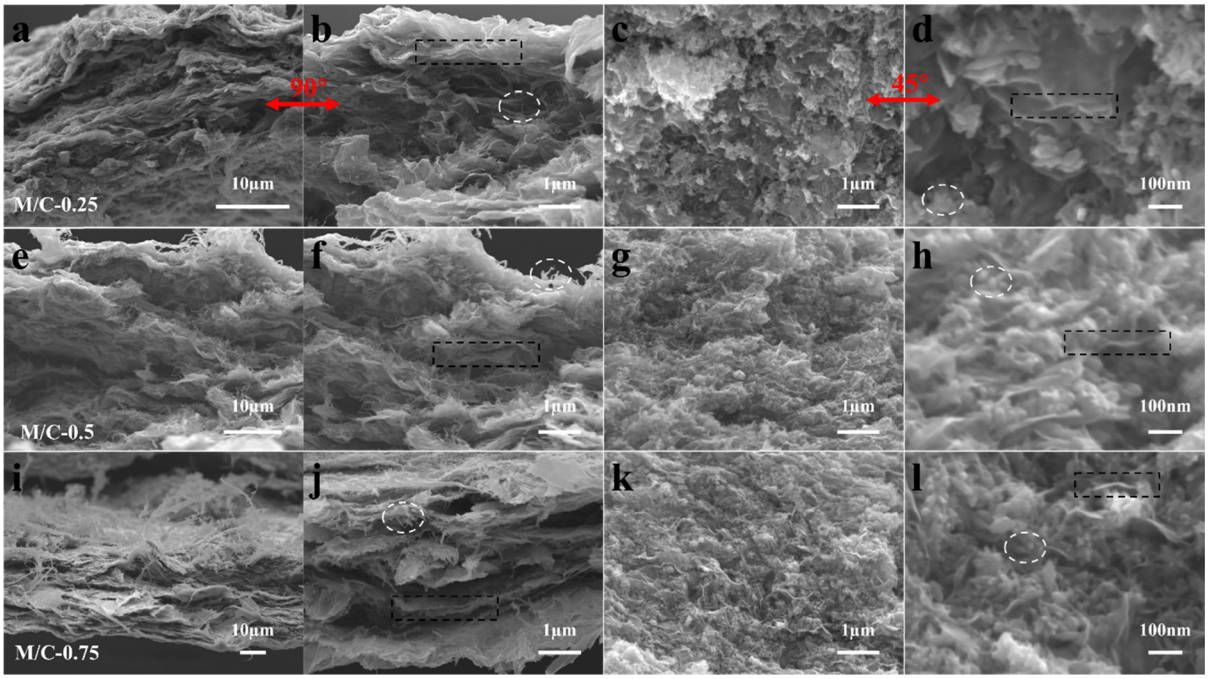

Fig. 2 SEM images of MXene/CNF composite films with different CNF loadings: (a)–(d) M/C-0.25, (e)–(h) M/C-0.5, and (i)–(l) M/C-0.75. For each group, cross-sectional images at different magnifications are shown in (a), (e) and (i) with 10 μm scale, (b), (f) and (j) with 1 μm scale, (c), (g) and (k) top-view at 45° with 1 μm scale, and (d), (h) and (l) top-view at high magnification with 100 nm scale. The area enclosed by the black rectangle in the figure is laminar Mxene, and the white circle is labeled CNF.

dispersed and intercalated in the MXene lamellae, which could overcome the brittleness of the MXene material itself and achieve a balance between flexibility and electrochemical properties. However, in the M/C-0.75 sample, excess CNFs lead to aggregation, which may destroy the excellent electrical conductivity and electrochemical properties of the MXene material itself.

This suggests that a suitable CNF mass ratio (M/C-0.5) can form a three-dimensional network while maintaining the ordered layered structure of MXene. It effectively balances the two important parameters of flexibility and electrochemical performance of MXene-based supercapacitors.

We further studied the composite films by physical characterization using XRD (shown in Fig. 3). As shown in the XRD patterns of pure MXene and MXene/CNF electrodes with different mass ratios (Fig. 3a), the characteristic peak of MXene (002) located at about 8° was observed for all samples. In addition, a new peak was observed in the XRD pattern corresponding to the CNF content, located at about 22.9°, indicating the presence of CNF fibers (Fig. 3a). As the mass ratio of added CNF fibers increases, the (002) peak on pure MXene, located at around 8.1°, shifts to a lower 2θ angle. Specifically, for M/C-0.25, M/C-0.5, and M/C-0.75 composite materials, the (002) peak shifts to about 7.2°, 7°, and 9°, respectively. This indicates a slight increase in the *c*-lattice parameter (*c*-LP) of MXenes/CNFs for fibers intercalated with appropriate levels of CNFs compared to pure MXene, with excess CNFs leading to a decrease.

The correlation between the *c*-lattice parameter (*c*-LP) and the CNF mass ratio was determined using eqn (1), based on the shift of the characteristic MXene (002) peak near 8° in the XRD pattern, as shown in Fig. 3b. The initial *c*-LP of the pristine MXene was approximately 22 Å. Upon the introduction of CNFs, the *c*-LP increased to around 24 Å for M/C-0.25 and further expanded to 26 Å for M/C-0.5. However, when the CNF mass ratio reached 75% (M/C-0.75), *c*-LP significantly dropped to below 20 Å. At lower CNF concentrations, the nanofibers intercalate evenly between MXene layers, enhancing interlayer spacing and promoting ion transport. In contrast, excessive CNF loading caused fiber aggregation, which hindered uniform dispersion, reduced interlayer spacing, and blocked ionic pathways—ultimately impairing the electrochemical performance of the composite. Nitrogen adsorption analysis further explains the variation of obtainable surface area with a change in CNF mass ratio. As shown in Fig. 3c, the highest nitrogen absorption was observed for the M/C-0.5 composites over the entire relative pressure range (p/p° = 0.05–0.30). This indicates that the appropriate amount of CNF intercalation prevents MXene stacking and expands the active area of the MXene material. The BET surface area results in Fig. 3d confirm this trend. The surface area of the dense, stacked laminar structure of the MXene (PM) was relatively low at 7.40 $m^2\ g^{-1}$. With the addition of 25% CNFs, the BET surface area increased to 9.57 $m^2\ g^{-1}$, which was attributed to the partial intercalation of the CNF. When 50% CNF was added (M/C-0.5), the BET surface area reached a maximum value of 15.78 $m^2\ g^{-1}$, which reflects the formation of an interconnected sandwich-like structure. However, by further increasing the CNF mass ratio to 75%, the surface area decreases significantly (10.69 $m^2\ g^{-1}$). This decrease agrees with the decrease in the c-lattice parameter

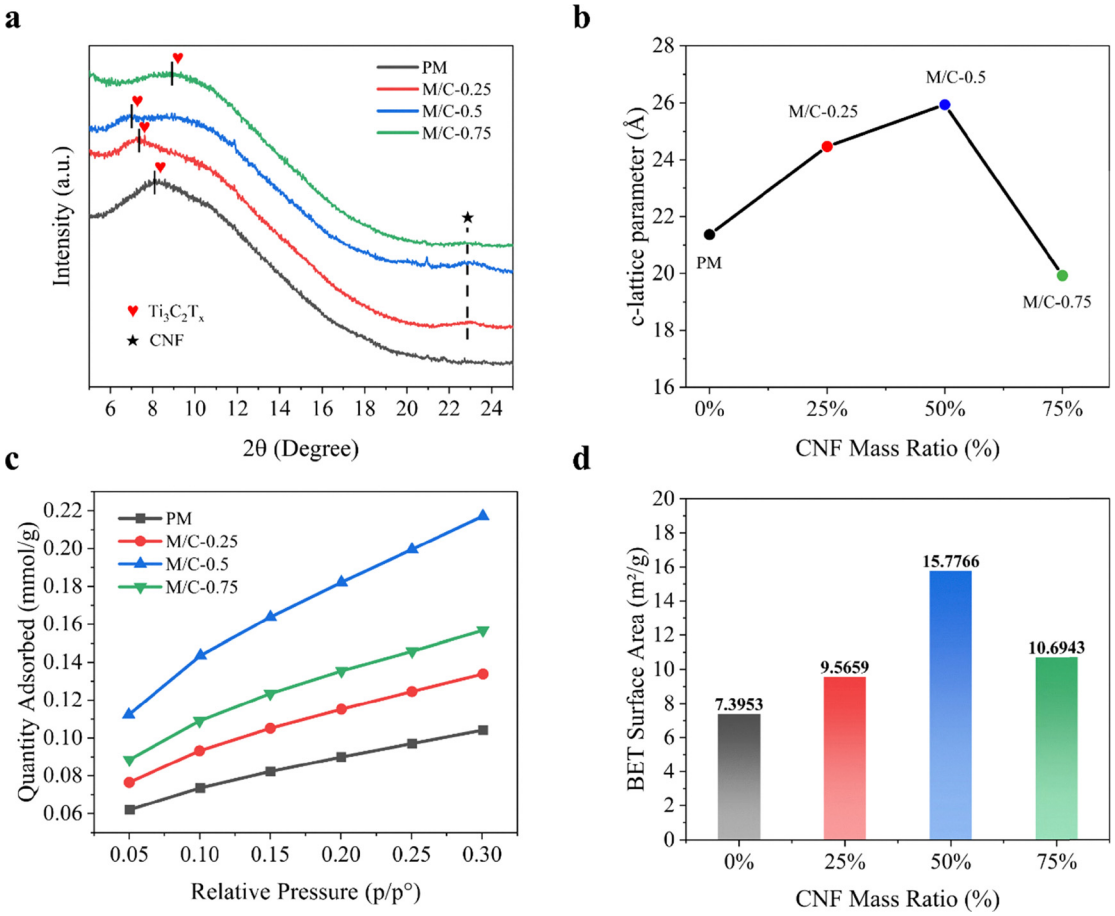

Fig. 3 (a) XRD data of PM, M/C-0.25, M/C-0.5 and M/C-0.75 composite thin films. (b) Calculated *c*-lattice parameter (c-LP) based on the XRD result. (c) Nitrogen adsorption isotherms in the low pressure region (0.05–0.3 relative pressure). (d) BET surface area of the samples.

and can be attributed to the blocking of ion channels due to CNF excess aggregation.

Electrochemical properties

In the initial stage of material optimization, an aqueous-based electrolyte was used. Its high ionic conductivity, simplicity and reproducibility facilitate rapid selection of different electrode compositions. Meanwhile, the aqueous system has been widely studied and is suitable for analyzing the charge storage mechanism and ion transport behaviour. Through these tests, we obtained key parameters and trends, which provide a reference for the further design of solid-state supercapacitors.

Aqueous MXene/CNF supercapacitor

For the aqueous MXene/CNF supercapacitor, the CV and GCD tests were carried out using 6 M KOH aqueous solution to evaluate the electrochemical properties of MXene/CNF composites.

The CV curves of all sample groups at 100 mV s^{-1} are shown in Fig. 4a. The CV curves of all the sample groups are nearly rectangular, indicating that they have good double-layer capacity and reversibility. In particular, the CV curves maintain their shapes at high scanning rates, demonstrating that the composites have an efficient charge transfer capability. However, M/C-0.25 and M/C-0.75 exhibited poor capacitive behaviour in the CV curves, whereas the M/C-0.5 hybrid film displayed a broader potential window, indicating enhanced electrochemical performance. Fig. 4b and c present the areal capacitance and volumetric capacitance of the films were calculated from the CV curves according to eqn (2). The areal capacitance and volumetric capacitance of the films show a gradual decrease when the voltage sweep rate is gradually increased from 5 mV s^{-1} to 100 mV s^{-1}. This is because the ions do not have enough time to be transported at a high scan rate. As shown in Fig. 4b, the M/C-0.5 samples show the highest area capacitance at all scan rates due to the enhanced ion transport by the coefficient of well-dispersed CNF and MXene. However, at higher scan rates (*e.g.* >80 mV s^{-1}), the bulk volumetric capacitance of PM samples is comparable to that of M/C-0.5. This can be explained by the higher packing density of the PM film, which overcomes the relatively low ion accessibility of the PM film at low scan rates. The compactness of the PM sample ensures that more active material is present per unit volume, which becomes even more important when the scan time is short and ion diffusion is limited. In contrast, the microstructure of the M/C-0.5 film is more porous due to the

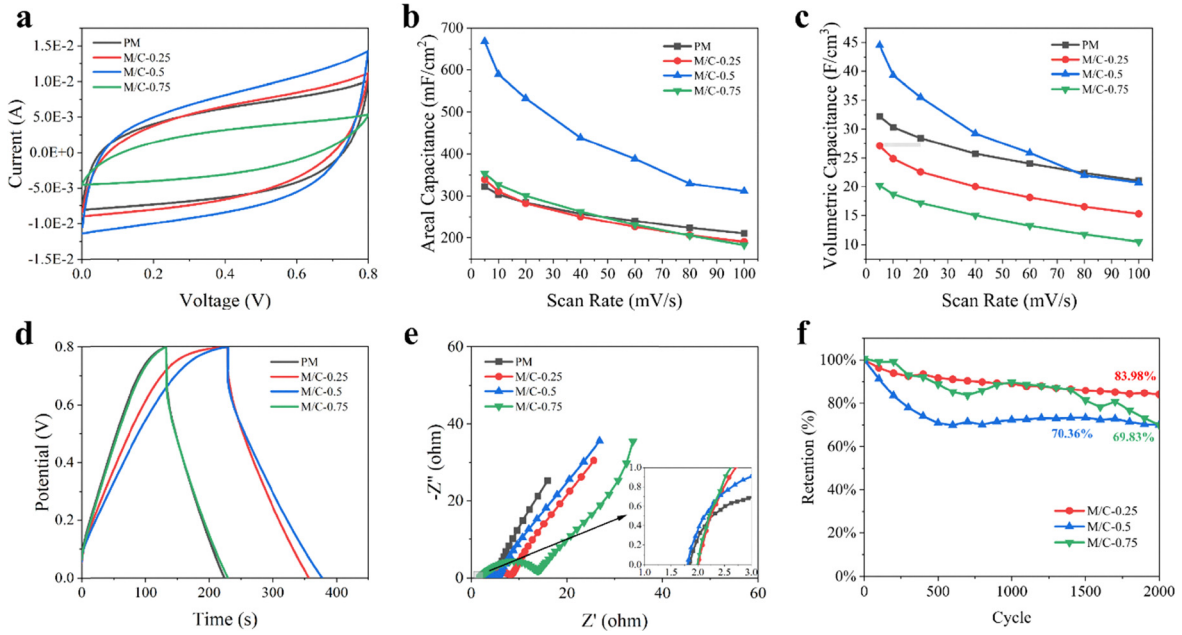

Fig. 4 Electrochemical properties of MXene and MXene/CNF composites: (a) CV curves of different materials at a scan rate of 10 mV s^{-1}; (b) plots of specific areal capacitance *versus* scan rate; (c) Plot of volume capacitance *versus* scan rate; (d) GCD curves at a current density of 1 mA cm^{-2}; (e) EIS in the frequency range of 100 kHz to 0.01 Hz, the inset is a zoomed-in view of the high-frequency region; (f) retention test of M/C samples at a current density of 3 mA cm^{-2}.

CNF intercalation, which improves ion transport at lower scan rates but reduces the overall packing density. This structural difference results in a higher area capacitance, but a slightly lower volume capacitance at high scan rates, where limited ion diffusion favors denser films. Overall, the M/C-0.5 hybrid film achieves the best capacitance performance in terms of areal capacitance and volumetric capacitance, respectively, of 668.12 mF cm^{-2} and 44.54 F cm^{-3} at a scan rate of 5 mV s^{-1}.

To further compare the electrochemical performance of different controls. Fig. 4d shows the GCD curves at a current density of 1 mA cm^{-2}. Different samples showed smooth and nearly linear curves. The discharge time gradually increased with the increase of cellulose fiber, and at a mass ratio higher than 50%, the discharge time decreased similarly to pure MXene. The longer discharge time indicates that the conductive material has a large areal-specific capacitance. However, there is a slight difference between the charging and discharging times, which suggests that the material is less stable during the charging and discharging process. The specific capacitances of PM, M/C-0.25, M/C-0.5, and M/C-0.75 were calculated to be 94.56, 127.53, 148.39, and 96.29 mF cm^{-2}, respectively. Among them, M/C-0.5 clearly delivers the highest capacitance. On the one hand, the MXene exhibits excellent electrical properties; on the other hand, with the CNF complex, open spaces can be formed between the MXene flakes to achieve rapid ion transport through the intercalation effect, resulting in more inaccessible surfaces on the MXene. Meanwhile, with the increase of CNF mass ratio, the accumulation of CNFs on the surface of MXene hindered ion transport; thus, 1 : 0.5 (MXene : CNFs) is the selected ratio.

Electrochemical impedance spectroscopy (EIS) is employed to analyze the charge storage kinetics in composite electrodes. Fig. 4e illustrates the Nyquist plots for all the samples. These plots consist of a high-frequency region and a low-frequency region. In the high-frequency region, a semicircular arc represents the charge transfer resistance (R_{ct}), while the low-frequency region is depicted as a straight line. The intersection of the curve with the real axis indicates the equivalent series resistance (R_s), which is approximately 2 ohms for all samples. The incorporation of CNFs enhances the intercalation of MXene nanosheets, creating pathways for charge carriers along the nanofibers and improving the diffusion of electrolyte ions in the electrodes. The R_{ct} value reflects the efficiency of charge transport at the electrode–electrolyte interface.[30] Among the tested samples, M/C-0.5 exhibited a significantly lower R_{ct} value compared to M/C-0.25 and M/C-0.75, indicating that the 1 : 0.5 MXene-to-CNF ratio was the most effective in facilitating interfacial charge transfer. This enhancement can be attributed to the more uniform dispersion of CNFs within the M/C-0.5 composite, which promotes the formation of a well-connected 3D network. Additionally, the CNFs effectively inhibit the restacking of MXene nanosheets, thereby improving the accessibility of electrolyte ions and shortening their transport pathways. In contrast, the lower CNF mass ratio in M/C-0.25 was insufficient to adequately fill the interlayer voids between MXene sheets, limiting ionic mobility. Meanwhile, the excessive CNFs in M/C-0.75 led to fiber aggregation, disrupting ion diffusion and increasing the overall electrochemical resistance.

Galvanostatic charge–discharge (GCD) cycling stability tests were performed on M/C-0.5 M/C-0.25, M/C-0.5, and M/C-0.75

for 2000 cycles at a current density of 3 mA cm^{-2} (Fig. 4f). Among these, the capacitance retention rate of M/C-0.25 was the highest, reaching 83.98%, while the retention rates of M/C-0.5 and M/C-0.75 were 70.36% and 69.83%, respectively. M/C-0.5 experienced rapid decay in the initial stage but stabilized around 70% after approximately 500 cycles, while M/C-0.75 exhibited a gradual degradation trend throughout the entire testing process (Fig. 4f). SEM and EDS mapping images taken before and after cycling were compared to investigate the cause of the capacitance drop in depth, particularly in M/C-0.5, as shown in Fig. S2. In Fig. S2a and b, the original composite film shows the crosslinked network structure of CNF intercalation into the lamellae of MXene, whereas the post-cycling samples show significant pore formation and localized delamination, suggesting that mechanical damage occurred during repeated ion insertion/extraction processes. Meanwhile, the 6 M KOH solution is a strong base, which may also cause structural damage to the MXene/CNF composite films. The EDS spectra (Fig. S2c and d) further confirmed the changes in elemental distribution. Weakened Ti and C signals and non-uniform dispersion, which may be due to the oxidation of the surfaces and partial loss of material. These structural and compositional changes disrupted the ionic/electronic pathways, leading to the capacitance decay (retention ~70%) observed after 2000 cycles. M/C-0.25 exhibits relatively good stability, which is attributed to its moderate CNF mass ratio, which strikes a balance between mechanical strength and interlayer ion transport. In contrast, the excessively high CNF mass ratio in M/C-0.75 may lead to uneven dispersion and aggregation, thereby impairing the 3D network and electrochemical performance during long-term cycling.

Flexible MXene/CNF SSCs

Through electrochemical tests in aqueous supercapacitors, the M/C-0.5 composite electrode material showed the relative best performance and achieved the highest volume specific capacitance (44.54 F cm^{-3}). Therefore, we selected the optimal ratio of 1 : 0.5 as the reference. Fig. 1 shows the fabrication process of the solid-state finger structured MXene/CNF electrode.

We designed and fabricated a precisely adjustable bending test fixture to evaluate the electrochemical performance of flexible supercapacitors under various bending conditions. The test platform consists of two symmetrical clamping plates connected by threaded rods, enabling precise control of the bending angle of the PET substrate held between them. As shown in Fig. 5a–d, the adjustment range is from 0° to 120°. Fig. 5e illustrates the bending morphology observed from the top, demonstrating that the platform can achieve repeatable symmetrical bending states. Fig. 5f shows a demonstration of the connection for testing finger-shaped supercapacitors. To enhance the hydrophilicity of the PET surface, the PET surface was treated with oxygen plasma before spin coating. As shown in Fig. S3, after plasma treatment, the contact angle of MXene/CNF droplets on the PET surface decreased significantly from 77.61° to 24.33°, providing an excellent contact surface for subsequent spin coating.

The microstructure of composite films prepared using different deposition methods was further compared *via* cross-sectional SEM (Fig. S4). Vacuum-filtered membranes (Fig. S4a and b) exhibited a 3D interwoven network, with CNFs uniformly intercalated within MXene, and an overall thickness of approximately 100 μm. In contrast, spin-coated membranes (Fig. S4c and d) featured uniformly dense, flat-layered structures, with MXene/CNFs interwoven and stacked together, while also providing a large surface area to facilitate ion transport, with an overall membrane thickness of approximately 10 μm. Cross-sectional images of spin-coated films were obtained after ion beam etching.

To evaluate the electrochemical performance and flexibility of MXene/CNF-based solid-state supercapacitors, we used two

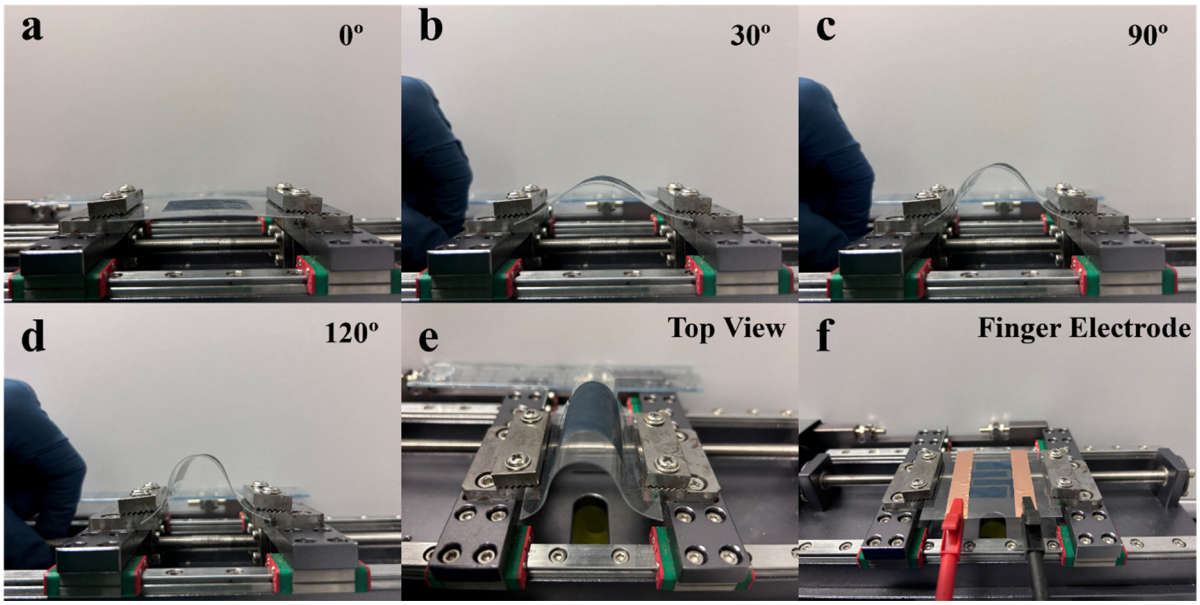

Fig. 5 Optical images of MXene/CNF SSCs: (a) 0°, (b) 30°, (c) 90°, (d) 120°, (e) top view of the device, and (f) final device demonstration test.

representative gel electrolytes: proton-conductive H_2SO_4/PVA and ionic liquid-based IL/PVA (EMIMAc). The devices were tested at different bending angles (flat, 30°, 60°, and 120°) to simulate real-world deformation scenarios in wearable electronics.

The cyclic voltammetry (CV) curves of MXene/CNF solid-state supercapacitors in both systems are shown in Fig. S5 and S6. Under all bending conditions, the shape of the CV curves remained close to rectangular, indicating excellent double-layer capacitance characteristics and reversibility at different bending angles (30°, 60°, and 120°). Notably, even at high scan rates, the CV curves retain their shape, indicating that the composite material exhibits efficient charge transfer capability. As shown in Fig. 6a and b, even at a low scan rate of 5 mV s^{-1}, the curves maintain an approximate rectangular shape, indicating ideal capacitive behaviour and excellent electrochemical reversibility. Under the same conditions, the H_2SO_4/PVA system exhibits a significantly higher current response compared to the IL/PVA system (Fig. 6b), attributed to the superior ionic conductivity and charge storage kinetics resulting from the high mobility of protons in H_2SO_4. In comparison, the IL/PVA system exhibits a wider electrochemical window (−0.5 V to 0.5 V), as shown in Fig. 6b, with a GCD charge–discharge voltage of 0.8 V. This is mainly attributed to the fact that EMIMAc is a non-protonic, non-aqueous ionic liquid, which prevents electrolyte decomposition during operation. This trend is further confirmed by the GCD curves (Fig. 6c and d), where the H_2SO_4/PVA system exhibits longer duration and more symmetrical curves during charging and discharging, especially under mild bending (94.21 F cm^{-3} at 30°), reflecting higher coulombic efficiency and lower internal resistance. However, there is an obvious sudden voltage drop in the GCD curve (Fig. 6c and d), indicating that the device has some internal resistance, especially at 120° bending. These phenomena are due to an increase in internal resistance under large-angle bending conditions and disturbance at the electrode–electrolyte interface, as confirmed by EIS data (Fig. 6g). Other researchers recommend that introducing high ionic conductivity PVA/H_3PO_4 gel electrolytes could improve the ion transport performance.[31] Meanwhile, reducing the CNF mass ratio could also increase the conductivity of the electrode. In contrast, the IL/PVA system exhibits a more triangular GCD shape and a higher initial voltage, despite

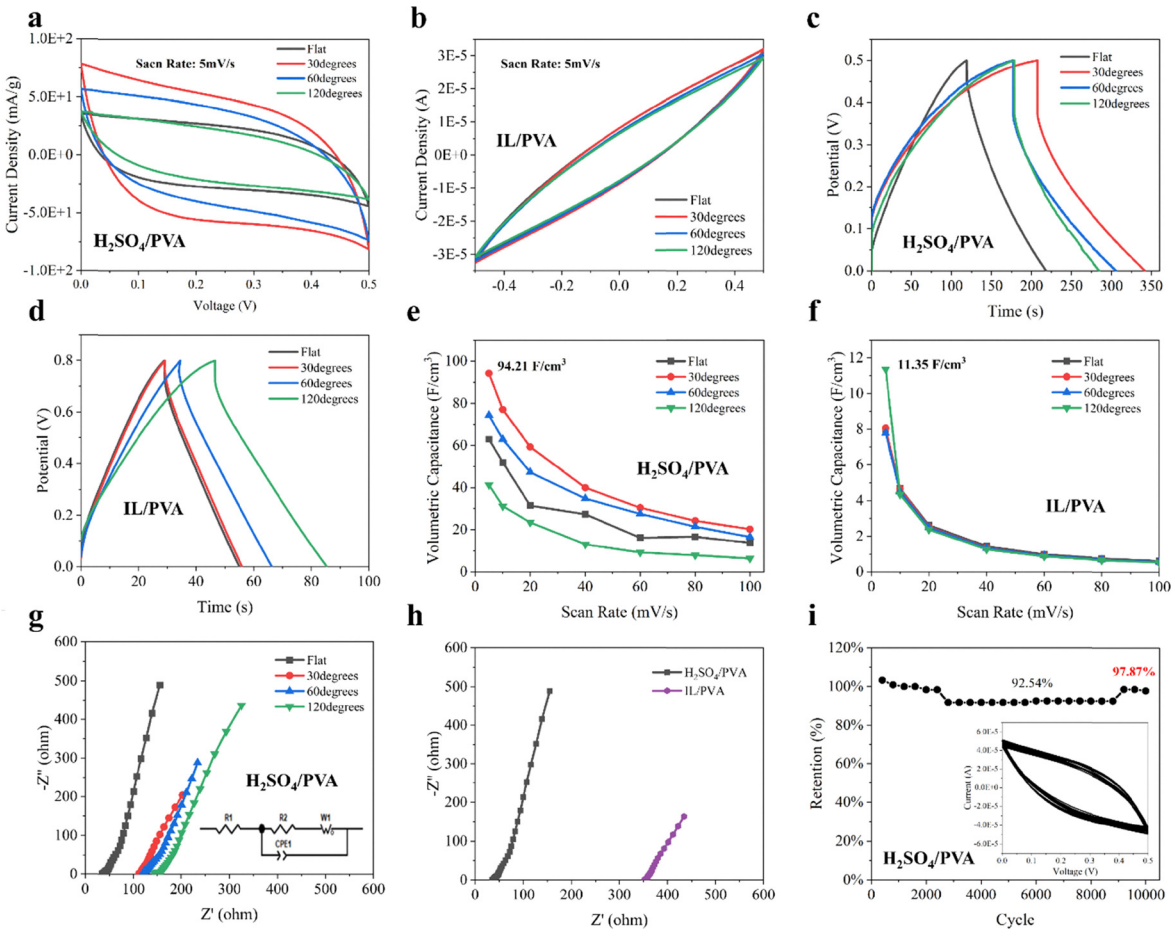

Fig. 6 Electrochemical performance of solid-state MXene/CNF symmetric supercapacitors using H_2SO_4/PVA and IL/PVA gel electrolytes at different bending angles (flat, 30°, 60°, and 120°). (a) and (b) CV comparison curves at a scan rate of 5 mV s^{-1}; (c) and (d) GCD curves at a current density of 1 mA cm^{-3}; (e) and (f) Plot of volume capacitance *versus* scan rate; (g) and (h) Nyquist plots and fitted equivalent circuit model (inset of g); and (i) retention test at 60° bending at a scan rate of 30 mV s^{-1} for 10 000 cycles.

a shorter discharge time, indicating stable double-layer capacitive behavior (Fig. 6g). However, its capacitance change (maximum value of approximately 11.35 F cm^{-3} at 120°) is relatively small (Fig. 6f), which may be attributed to the high viscosity and low ionic mobility of the ionic liquid.

Under flat conditions, we performed GCD electrochemical testing of the H_2SO_4/PVA system, as shown in Fig. S7b. The volumetric energy density of the H_2SO_4/PVA system can be up to 2.1 mWh cm^{-3} and the power density can be up to 0.25 W cm^{-3} as calculated by eqn (4) and (5). Through further electrochemical performance tests and upon analyzing the measured data, as shown in Fig. 6e and f, the H_2SO_4/PVA system shows relatively better performance in energy storage. We found that the interfacial contact of the H_2SO_4/PVA system is optimized at slight bends (30° and 60°), resulting in a smoother ion transport path and a significant improvement in performance. At 30° bending, the mass specific capacitance reaches 20.09 F g^{-1} (Fig. S7a), the volume specific capacitance is 94.21 F cm^{-3}, and the energy density of the electrodes is 3.27 mWh cm^{-3}. The above data were calculated based on CV curves at a scan rate of 5 mV s^{-1}. The mass specific capacitance and volume specific capacitance are calculated using eqn (2) and the energy density is obtained using eqn (4). Impedance analysis (Fig. 6g and h) further confirmed these observations: H_2SO_4/PVA exhibited lower charge transfer resistance under moderate bending (30°–60°), which may indicate an improved electrolyte–electrode interface under mild deformation, thereby enhancing ion transport. In contrast, the IL/PVA system showed relatively high resistance, consistent with a lower capacitance output.

The Nyquist plot (Fig. 6g and h) shows that the Nyquist plot exhibits an approximately linear trend in the low-frequency region and does not exhibit a distinct semicircular region in the high-frequency region, indicating that the MXene/CNF solid-state supercapacitor operates based on electric double-layer capacitance (EDLC) behaviour. The initial intersection point with the real axis in the high-frequency region corresponds to the series internal resistance (R_s) of the device, primarily composed of an electrode, an electrolyte, and interfacial contact resistances. In the H_2SO_4/PVA system (Fig. 6g), the Nyquist curve in the low-frequency region exhibits a slightly curved trend, indicating the presence of ion diffusion impedance in the electrode. As the bending angle gradually increases from the flat state to 120°, the slope of the Nyquist curve gradually decreases, and the total impedance significantly increases (Fig. 6g). The increased Z' and Z'' values observed at higher bending angles (especially 120°) indicate that mechanical deformation causes microstructural damage or partial peeling, blocking ion transport pathways (Fig. 6g). Comparing the two electrolytes, the overall impedance and diffusion limitation of IL/PVA are significantly higher than those of H_2SO_4/PVA. This may be attributed to the lower ionic conductivity of the ionic liquid gel system and the higher viscosity of EMImAc, which restricts ion migration within the solid matrix. The equivalent circuit model in Fig. 6g includes: R_s (series internal resistance), R_{ct} (charge transfer resistance), C_{dl} (double-layer capacitance), and Warburg element (W_0). Overall, bending exacerbates charge transfer impedance, and the IL/PVA electrolyte, due to its inherently poor ionic mobility, exhibits higher total impedance in solid-state devices. In contrast, the H_2SO_4/PVA gel electrolyte has lower internal resistance and higher conductivity, making it more suitable for high-rate charging and discharging scenarios. While IL/PVA serves as a reference comparison with a broader electrochemical window, its limited ion mobility restricts rate performance.

Cycling stability is a critical metric for flexible energy storage, evaluated through repeated bending tests (Fig. 6i). Surprisingly, the H_2SO_4/PVA-based device retained 97.87% of its initial capacitance after 10 000 cycles under 60° bending conditions (inset shows CV tests for the first and last 50 cycles), demonstrating excellent electrochemical durability and mechanical toughness. The IL/PVA system maintained a capacitance retention rate of 75.83% after 5000 cycles (Fig. S8).

In flexible wearable application scenarios, the bending angle of different parts of the human body varies, for example, the bending angle of the wrist is about 30°–60°, while the knees and elbows can reach about 120° in daily activities.[32] Therefore, the device shows excellent electrochemical performance and mechanical stability in most flexible wearable device scenarios and has a wide range of application potential.

Several devices were fabricated to further validate SSCs for real-world applications as portable storage devices (H_2SO_4/PVA gel electrolyte). The effects of their electrochemical properties are discussed through both series and parallel connections, and their application potential is verified by lighting a red LED. Fig. 7a and b present a comparison of the CV curves of a single cell with those of two cells in series or parallel connections, and show that series connections increase the output voltage, while parallel connections increase the output current, providing tunability for different application requirements. Fig. 7c shows the discharge curves of a single cell *versus* two cells connected in parallel at a charge density of 10 mA cm^{-3}. The shunt configuration extends the discharge time, indicating a higher energy storage capacity, which contributes to the range performance. Fig. 7d further shows the CV variation for 1 to 5 series cells, with cyclic voltammetry (CV) measurements performed at a scan rate of 100 mV s^{-1}. As the number of series cells increases, the open-circuit voltage increases significantly, indicating that the device can regulate the output voltage by series connection to meet the needs of different electronic devices. Fig. 7e shows the charging and discharging curves of five series-connected batteries at different charging voltages (0–2.5 V, 0–4 V, and 0–5 V), verifying the energy storage capability of the device and showing that the power supply performance can be optimized by charging voltage. It is also demonstrated that the MXene/CNF SSC can withstand larger charging voltages (less than 1 V), so the use of three capacitors in series can theoretically satisfy the operating requirements of LEDs (20 mA, 2.7 V). Finally, Fig. 7f shows the practical application of the flexible energy device, where an LED lamp was successfully driven using five series-connected flexible electrodes, demonstrating its potential application in smart devices such as wearable electronics and flexible sensors (Fig. S9 and Video S1).

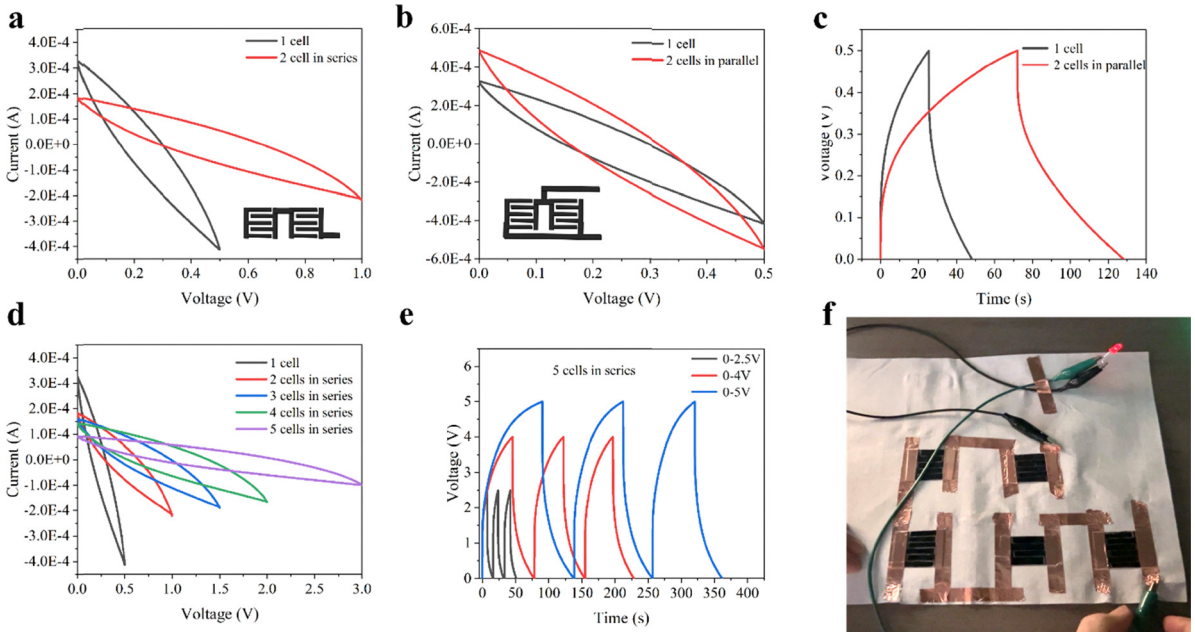

Fig. 7 CV curves of a single cell in series (a) and in parallel (b) for different voltage ranges (scan rate, 100 mV s^{-1}). (c) Charge and discharge characteristics of a single cell *versus* two cells connected in parallel (charge density, 10 mA cm^{-3}). (d) CV characteristics of different numbers (1 to 5) of cells in series (scan rate, 100 mV s^{-1}). (e) Charge/discharge (charge density, 10 mA cm^{-3}) curves for 5 cells in series with different charging voltages (0–2.5 V, 0–4 V, and 0–5 V). (f) Illuminated red LEDs using all solid-state supercapacitors.

The flexible thin-film supercapacitors prepared in this work exhibit good overall performance between energy density and power density, as shown in the Ragone plot in Fig. 8. The device's volumetric energy density reaches up to 3.27 mWh cm^{-3} and the power density reaches up to 0.25 W cm^{-3}, which has a significant advantage over the commercially available 5.5 V/100 mF supercapacitors and most of the carbon-based or MXene-based flexible devices reported in the literature (ref. 33–40). This excellent performance is due to the optimized thin film structure (~100 μm thickness) with fast ion/electron transport channels. The device performance is significantly better than that of conventional capacitors, approaching the region of lithium film batteries, and demonstrating a promising application in the field of wearable energy devices. The direct quantitative comparison data are shown in Table S3.

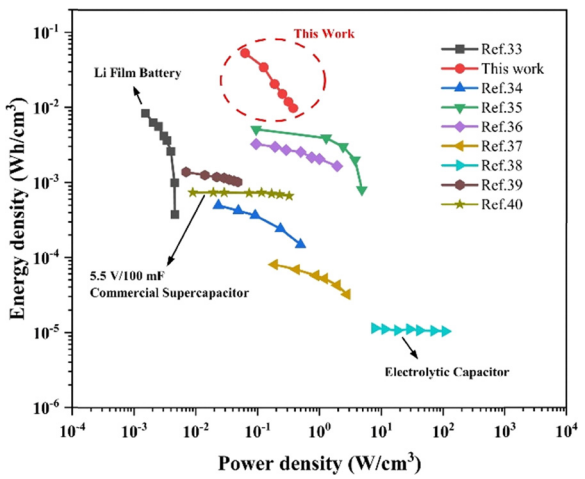

Fig. 8 Ragone plots that compare the energy and power densities of micro/solid state flexible supercapacitors with those of commercial electrolytic capacitors, supercapacitors, and Li thin-film battery energy storage devices.[33–40]

Conclusion

In summary, through the incorporation of CNF intercalation and the optimization of MXene/CNF composite electrodes, a flexible SSC was successfully fabricated. The innovative design significantly improved the structural integrity and electrochemical performance of the device, achieving a remarkable volumetric capacitance of 94.21 F cm^{-3} and retaining 97.87% of its capacitance after 10 000 bending cycles at an angle of 60°. The SSC demonstrated high stability and excellent energy storage performance across various bending states (flat, 30°, 60°, and 120°), showcasing its adaptability to dynamic mechanical deformations. The device achieves a volumetric energy density of up to 3.27 mWh cm^{-3} and a power density of up to 0.25 W cm^{-3} in the 30° bending state. Furthermore, the precise electrode engineering and solid-state electrolyte integration enabled reliable performance suitable for wearable and portable applications. This study highlights the promising potential of MXene/CNF-based SSCs as high-performance energy storage devices compatible with next-generation flexible electronics, including wearable sensors and IoT devices.

Conflicts of interest

There are no conflicts to declare.

Data availability

The data that support the findings of this study are available from the corresponding author upon reasonable request. Additional experimental data, characterization results, and device demonstration videos are provided in the Supplementary Information file.

Supplementary information is available. See DOI: **https://doi.org/10.1039/d5nh00285k**.

Acknowledgements

Y. A. W. acknowledges the Tang Family Chair Professorship for funding.

References

1 M. Lukatskaya, O. Mashtalir, C. E. Ren, Y. Dall'Agnese, P. Rozier, P. Taberna, M. Naguib, P. Simon, M. Barsoum and Y. Gogotsi, *Science*, 2013, **341**, 1502–1505.
2 F. Li, Y.-L. Liu, G.-G. Wang, H.-Y. Zhang, B. Zhang, G.-Z. Li, Z.-P. Wu, L.-Y. Dang and J.-C. Han, *J. Mater. Chem. A*, 2019, **7**, 22631–22641.
3 K. Yang, M. Luo, D. Zhang, C. Liu, Z. Li, L. Wang, W. Chen and X. Zhou, *Chem. Eng. J.*, 2022, **427**, 132002.
4 M. Zhao, C. E. Ren, Z. Ling, M. Lukatskaya, C. Zhang, K. L. V. Aken, M. Barsoum and Y. Gogotsi, *Adv. Mater.*, 2015, **27**, 339–345.
5 S. Li, L. D. Xu and S. Zhao, *Inf. Syst. Front.*, 2015, **17**, 243–259.
6 B. L. Risteska Stojkoska and K. V. Trivodaliev, *J. Cleaner Prod.*, 2017, **140**, 1454–1464.
7 S. Kumar, P. Tiwari and M. Zymbler, *J. Big Data*, 2019, **6**, 111.
8 M. Zhu, Y. Huang, Q. Deng, J. Zhou, Z. Pei, Q. Xue, Y. Huang, Z. Wang, H. Li, Q. Huang and C. Zhi, *Adv. Energy Mater.*, 2016, **6**, 1600969.
9 J. Yan, C. E. Ren, K. Maleski, C. Hatter, B. Anasori, P. Urbankowski, A. Sarycheva and Y. Gogotsi, *Adv. Funct. Mater.*, 2017, **27**, 1701264.
10 K. R. G. Lim, M. Shekhirev, B. C. Wyatt, B. Anasori, Y. Gogotsi and Z. W. Seh, *Nat. Synth.*, 2022, **1**, 601–614.
11 M. Naguib, O. Mashtalir, J. Carle, V. Presser, J. Lu, L. Hultman, Y. Gogotsi and M. Barsoum, *ACS Nano*, 2012, **6**(2), 1322–1331.
12 J. Orangi, F. Hamade, V. A. Davis and M. Beidaghi, *ACS Nano*, 2020, **14**, 640–650.
13 W. Yang, J. Yang, J. J. Byun, F. P. Moissinac, J. Xu, S. J. Haigh, M. Domingos, M. A. Bissett, R. A. W. Dryfe and S. Barg, *Adv. Mater.*, 2019, **31**, 1902725.
14 G. Zhou, M.-C. Li, C. Liu, Q. Wu and C. Mei, *Adv. Funct. Mater.*, 2022, **32**, 2109593.
15 G. Zhou, X. Liu, C. Liu, Z. Li, C. Liu, X. Shi, Z. Li, C. Mei and M.-C. Li, *J. Mater. Chem. A*, 2024, **12**, 3734–3744.
16 D. D. Khumujam, T. Kshetri, T. I. Singh, N. H. Kim and J. H. Lee, *Chem. Eng. J.*, 2022, **449**, 137732.
17 Q. Yang, Z. Xu, B. Fang, T. Huang, S. Cai, H. Chen, Y. Liu, K. Gopalsamy, W. Gao and C. Gao, *J. Mater. Chem. A*, 2017, **5**, 22113–22119.
18 H. Zhang, Y. Luo, J. Zhou, L. Wang, L. Shu, W. He, Q. Zhang and P. Wang, *Nano Lett.*, 2024, **24**, 10131–10138.
19 J. Zhang, S. Seyedin, S. Qin, Z. Wang, S. Moradi, F. Yang, P. A. Lynch, W. Yang, J. Liu, X. Wang and J. M. Razal, *Small*, 2019, **15**, 1804732.
20 M. Hu, T. Hu, R. Cheng, J. Yang, C. Cui, C. Zhang and X. Wang, *J. Energy Chem.*, 2018, **27**, 161–166.
21 L. Wang, D. Shao, J. Guo, S. Zhang and Y. Lu, *Energy Technol.*, 2020, **8**, 1901003.
22 M. Boota, B. Anasori, C. Voigt, M. Zhao, M. Barsoum and Y. Gogotsi, *Adv. Mater.*, 2016, **28**, 1517–1522.
23 L. Yang, F. Lin, F. Zabihi, S. Yang and M. Zhu, *Int. J. Biol. Macromol.*, 2021, **181**, 1063–1071.
24 C. Couly, M. Alhabeb, K. L. Van Aken, N. Kurra, L. Gomes, A. M. Navarro-Suárez, B. Anasori, H. N. Alshareef and Y. Gogotsi, *Adv. Electron. Mater.*, 2018, **4**, 1700339.
25 J. Lee, W. Kim and W. Kim, *ACS Appl. Mater. Interfaces*, 2014, **6**, 13578–13586.
26 S. P. Sreenilayam, I. Ul Ahad, V. Nicolosi and D. Brabazon, *Mater. Today*, 2021, **43**, 99–131.
27 D. Qi, Y. Liu, Z. Liu, L. Zhang and X. Chen, *Adv. Mater.*, 2017, **29**, 1602802.
28 S. Jiao, A. Zhou, M. Wu and H. Hu, *Adv. Sci.*, 2019, **6**, 1900529.
29 M. Ghidiu, M. R. Lukatskaya, M.-Q. Zhao, Y. Gogotsi and M. W. Barsoum, *Nature*, 2014, **516**, 78–81.
30 P. L. Taberna, P. Simon and J. F. Fauvarque, *J. Electrochem. Soc.*, 2003, **150**, A292.
31 S. Alipoori, S. Mazinani, S. H. Aboutalebi and F. Sharif, *J. Energy Storage*, 2020, **27**, 101072.
32 I. P. Herman, *Physics of the Human Body*, Springer, 2016.
33 D. Pech, M. Brunet, H. Durou, P. Huang, V. Mochalin, Y. Gogotsi, P.-L. Taberna and P. Simon, *Nat. Nanotechnol.*, 2010, **5**, 651–654.
34 F. Wen, C. Hao, J. Xiang, L. Wang, H. Hou, Z. Su, W. Hu and Z. Liu, *Carbon*, 2014, **75**, 236–243.
35 L. Zhang, G. Yang, Z. Chen, D. Liu, J. Wang, Y. Qian, C. Chen, Y. Liu, L. Wang, J. Razal and W. Lei, *J. Materiomics*, 2020, **6**, 138–144.
36 Y. Xie, H. Zhang, H. Huang, Z. Wang, Z. Xu, H. Zhao, Y. Wang, N. Chen and W. Yang, *Nano Energy*, 2020, **74**, 104928.
37 M. F. El-Kady and R. B. Kaner, *Nat. Commun.*, 2013, **4**, 1475.
38 M. F. El-Kady, V. Strong, S. Dubin and R. B. Kaner, *Science*, 2012, **335**, 1326–1330.
39 S. Deshmukh, K. Ghosh, M. Pykal, M. Otyepka and M. Pumera, *ACS Nano*, 2023, **17**, 20537–20550.
40 Y. Yuan, L. Jiang, X. Li, P. Zuo, X. Zhang, Y. Lian, Y. Ma, M. Liang, Y. Zhao and L. Qu, *Adv. Mater.*, 2022, **34**, 2110013.

